



Communication

Insights of Fe₂O₃ and MoO₃ Electrodes for Electrocatalytic CO₂ Reduction in Aprotic Media

Néstor E. Mendieta-Reyes ¹, Alejandra S. Lozano-Pérez ¹ and Carlos A. Guerrero-Fajardo ^{1,*}

Departamento de Química, Facultad de Ciencias, Universidad Nacional de Colombia, Bogotá 11321, Colombia

* Correspondence: caguerrero@unal.edu.co; Tel.: +57-3164308909

Abstract: Transition metal oxides (TMO) have been successfully used as electrocatalytically active materials for CO₂ reduction in some studies. Because of the lack of understanding of the catalytic behavior of TMOs, electrochemical methods are used to investigate the CO₂ reduction in thin-film nanostructured electrodes. In this context, nanostructured thin films of Fe₂O₃ and MoO₃ in an aprotic medium of acetonitrile have been used to study the CO₂ reduction reaction. In addition, a synergistic effect between CO₂ and the TMO surface is observed. Faradic cathodic processes not only start at lower potentials than those reported with metal electrodes, but also an increase in capacitive currents is observed, which is directly related to an increase in oxygen vacancies. Finally, the results obtained show CO as a product of the reduction.

Keywords: CO₂ reduction; TMO electrodes; electrocatalysis; dissociative electroreduction model



Citation: Mendieta-Reyes, N.E.; Lozano-Pérez, A.S.; Guerrero-Fajardo, C.A. Insights of Fe₂O₃ and MoO₃ Electrodes for Electrocatalytic CO₂ Reduction in Aprotic Media. *Int. J. Mol. Sci.* **2022**, *23*, 13367. <https://doi.org/10.3390/ijms232113367>

Academic Editor: Jing Yu

Received: 6 September 2022

Accepted: 16 October 2022

Published: 2 November 2022

Publisher's Note: MDPI stays neutral with regard to jurisdictional claims in published maps and institutional affiliations.



Copyright: © 2022 by the authors. Licensee MDPI, Basel, Switzerland. This article is an open access article distributed under the terms and conditions of the Creative Commons Attribution (CC BY) license (<https://creativecommons.org/licenses/by/4.0/>).

1. Introduction

The current atmospheric levels of carbon dioxide and the depletion of fossil fuel reserves raise serious concerns about the resulting effects on the global climate change and on the future of some energy sources [1]. The electrochemical conversion of carbon dioxide is a promising way to address both problems simultaneously; this strategy provides an opportunity for the supply of platform chemicals, which can be used as supplementary raw materials in several industrial processes, or energy sources [2]. A wide variety of methods, such as photocatalysis, electrocatalysis, and heterogeneous catalysis, have all been successful in CO₂ reduction [3]. Factors such as solvent, electrolyte, pH, temperature, CO₂ concentration, electrode material, surface structure, and electrode potential influence the variety of products obtained [4,5]. Reduction products, including CO, CH₄, and CH₃OH, among others, have been reported [6–8]. This leads to the development of several reaction mechanisms with different numbers of electrons transferred, which determines the final oxidation state of the carbon atom [9]. However, due to the linear geometry with a closed-shell electronic configuration, the high energy level of its LUMO, and the low electron affinity of the molecule (0.6 eV), the reduction of CO₂ is a non-spontaneous reaction requiring an energy input. Due to the repulsion between the newly acquired electron and the free electron pairs on the oxygen atoms, the transfer of an electron results in the formation of the anion radical CO₂⁽⁻⁾, which causes the molecular structure to bend [10–13].

In this sense, several reports have shown that the stabilization of the CO₂⁽⁻⁾ anion radical is an important step for achieving an efficient reduction of CO₂. The CO₂ molecule can then be activated on a solid-state catalyst, whose function is to adsorb the CO₂ molecules by facilitating electron transference from the catalyst, providing favorable conditions for the bending of the molecule and the desorption of the products [10,11,14,15]. In this regard, the adduct formation of CO₂^(δ,-) on different metal oxides has been widely reported [16,17].

On the other hand, in an aqueous solution, different factors, such as acid-base equilibria and hydrogen synthesis occurring as a competitive process, act against obtaining

high efficiency and selectivity. In this sense, acetonitrile (ACN) is one of the most widely used non-aqueous aprotic solvents in catalysis and electrochemistry, and has been used to study the electrocatalytic CO₂ reduction [18–20]. Pons et al. studied solutions of tetrabutylammonium tetrafluoroborate (TBAF) in dry ACN, finding ACN decomposition at potentials more negative than -3.0 V vs. Ag/Ag⁺ (0.01 M) [5]. The ACN solution containing tetrabutylammonium salts, such as the electrolyte system, TBAF (0.1 M), has been used for the study of the electrocatalytic reduction of CO₂. This non-aqueous system not only offers stability at a potential window more negative than -1.97 V vs. SHE, which is needed for the first CO₂ electron transfer, but also that avoids the hydrogen synthesis as a competitive reaction.

Metal oxides are used as electrocatalysts for CO₂ reduction [21], and transition metal oxides (TMO) have been theoretically predicted to have efficient active sites for said reduction reaction [22]. In fact, these materials have reactive electrons, empty d orbitals, and crystalline defects, such as oxygen vacancies (OV), grain boundaries, and non-stoichiometry, that are capable of triggering the CO₂ molecule activation, inducing the formation of the CO₂^(δ⁻) adduct [11]. Compared with metal catalysts, TMO can further improve the performance of CO₂ reduction, which has drawn attention in recent studies. Some researchers have proposed that the active sites for CO₂ in metal oxides are due to the reconstruction of their surface, formed by the reduced surface of the metal oxide at highly negative operating potentials [23], whereas others have highlighted metal-oxygen sites as active, leaving an open debate on this topic [24]. In this context and based on the dissociative reduction model previously reported for CO₂ conversion at WO₃ and TiO₂ electrodes, results on Fe₂O₃ and MoO₃ electrodes are shown for the CO₂ electrochemical reduction. These findings provide an explanation for the electrocatalytic activity seen in other TMOs that have been previously studied, as well as their relationship with surface processes and the formation of OV, in terms of cathodic current and the initial potential that is related to CO₂ reduction [25–27].

2. Results and Discussion

Fe₂O₃ and MoO₃ thin-film electrodes were coated on Fluorine-doped Tin Oxide (FTO) substrates following two different synthesis routes, as explained in the Supplementary Information, leading to different morphologies. Synthesized Fe₂O₃ thin-film surface characterization is shown as to hematite, and a highly coated nanostructured electrode surface displaying 50 nm-thick nanoparticles is observed (Figure S2). An oxide film cross-section image, with approximately 500 nm-thickness, shows partially oriented nanobars. FE-SEM images for MoO₃ electrodes, at two different magnification levels of 5000× and 25,000×, are shown in Figure S3. Electrodes prepared by sol-gel process are thoroughly coated, with no uncoated substrate areas (Figure S3a). The morphology of the nanoparticles (Figure S3b) is in accordance with electrodes synthesized by the sol-gel technique. The observed nanoparticles' diameter is between 20–40 nm, with crystal aggregates well interconnected with each other. The X-ray diffraction pattern of the FTO-coated thin-film electrodes presented in Figure S4 indicates that the as-prepared product presents high-crystallinity.

For electrochemical studies, the prepared electrodes were evaluated in a 0.1 M tetrabutylammonium perchlorate (TBAP)/ACN solution as the supporting electrolyte. The electrolyte solution was purged with CO₂ and N₂ for 30 min before the electrochemical procedure. Figure 1 shows the voltametric response for both the Fe₂O₃ and MoO₃ working electrodes. The potential window for CO₂ reduction was determined by purging with N₂. Both Fe₂O₃ and MoO₃ electrodes show an increase in the cathodic current, with an onset at around -0.4 V and -0.6 V, respectively, which coincides with the beginning of the accumulation region. From a chemical point of view, such an increase can be seen as corresponding to Fe_(ss)(III)/(II) and Mo_(ss)(VI)/(V) redox processes in surface sites for Fe₂O₃ and MoO₃ (indicated on the figure). Similar behavior has been observed in semiconductor materials such as TiO₂ [28].

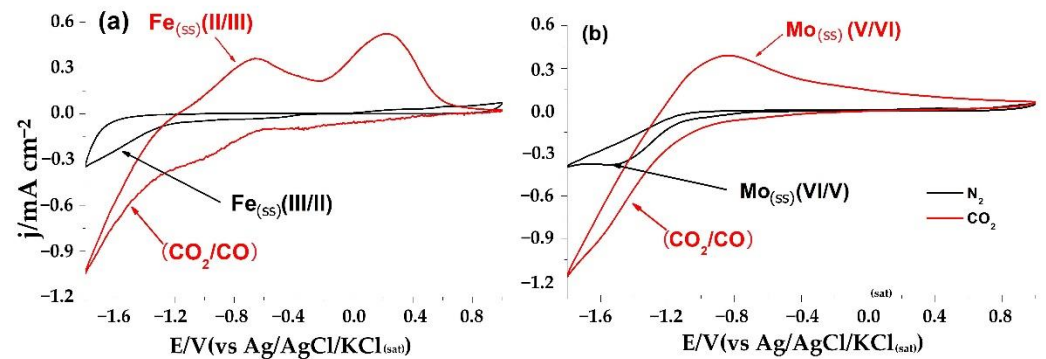
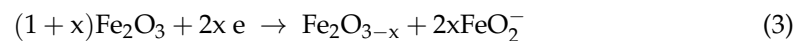
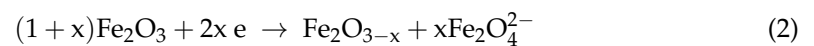
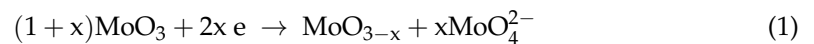


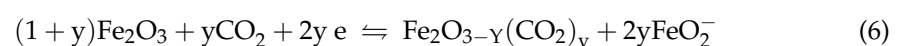
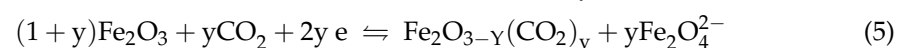
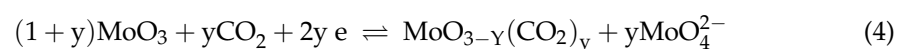
Figure 1. Cyclic voltammograms for CO₂ reduction over thin-film electrodes: (a) Fe₂O₃ and (b) MoO₃ in 0.1 M TBAF/ACN electrolyte solutions; black and red plots correspond to CO₂ and N₂ purged electrolytes, respectively. (ss) corresponds to metal atoms in surface states.

It has been reported that the metal reduced species in TMOs could be stabilized by small cations, such as H⁺ or Li⁺, through intercalation processes by local bronze formation [29]. However, in our case, one should bear in mind that the tetrabutylammonium cation (TBA⁺) is bulkier than the cavity available in the crystal lattice of metal oxide. Thus, TBA⁺ is sterically obstructed for intercalation. This fact not only acts in favor of OV formation, but also, the stabilization of the Fe_(ss)(II) and Mo_(ss)(V) metal surface centers with high electron density is not efficient. This is according with the previously reported dissociative electroreduction model [30]. Under these conditions, there is an increase in surface states energetically located close to the conduction band, and the OV formation is represented by the following equations:

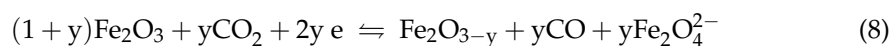
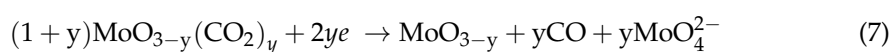


In this dissociative model, the partial electroreduction of MO₃ and Fe₂O₃ is limited to the interfacial region, whereas no significant structural damage occurs in the underlying region of the metal oxide film. According to Equations (1) and (3), the partial electroreduction of Mo and Fe lattice atoms from Mo⁶⁺ to Mo⁵⁺ and Fe³⁺ to Fe²⁺ induces the formation of oxygen-deficient metal oxide, MoO_{3-x} and Fe₂O_{3-x}. Additionally, this mechanism entails a loss of mass due to the electrodisolution of MoO₃ and Fe₂O₃ by the formation of MoO₄²⁻ and FeO₂⁻ [31].

Under the CO₂ purged condition, faradaic currents at −0.6 V and −0.8 V are observed for Fe₂O₃ and MoO₃, respectively. In both cases, the presence of CO₂ increased the electrode capacitance, even at potentials where CO₂ reduction does not occur. This fact suggests important changes in the electrode state that could be associated with an increase in the surface density of Mo⁺⁵- and Fe⁺²-reduced species as a result of the enhancement of the OV generation. This makes the potential at the onset of the reduction of metal atoms at TMO and the cathodic current associated with CO₂ reduction indistinguishable. The increase in the capacitive current has been explained in terms of the increment of OV promoted by increasingly negative applied potential, which favors CO₂ electro adsorption according to the equations:



The adsorption of CO₂ would, thus, promote the generation of non-stoichiometric Fe₂O_(3-y)(CO₂)_y and MoO_(3-y)(CO₂)_y. In this sense, the adsorption of CO₂ induces the stabilization of reduced metal sites. The results show that CO₂ binds slightly more strongly to stoichiometrically Ti(III)-deficient sites than to Ti(IV) sites, according to CO₂ adsorption studies on TiO₂. Therefore, it is reasonable to assume that CO₂ adsorption is favored at reduced metal sites (Mo(V) and Fe(II)). Thus, a synergistic effect between CO₂ and surface sites is verified. CO₂ adsorption not only activates the molecule by the adduct formation, but also induces a promotion of OV and the electron-rich center formation in reduced metal species. By further reducing the applied potential, the resulting high concentration of electrons located in the near-surface region would facilitate charge transfer from the electrode to the adsorbed CO₂ molecules, leading to the appearance of faradaic currents. It is worth noting that CO has been detected by gas chromatography analysis (presented in Figure S1 in Supporting Information), and the formation proceeds with two electrons transferred, according to Equations (7) and (8):



In the positive-going scan, a pseudocapacitive peak related to the reoxidation of the reduced metal is observed, and an enhancement in the electrode capacitance related to the increase in reduced metal sites Fe_(ss)(II)/(III) and Mo_(ss)(V)/(VI) is evident. Moreover, in the case of Fe₂O₃, an additional peak, probably related to the reoxidation of some CO₂ reduction product, appears at 0.3 V. This fact is intriguing because it demonstrates that each metal oxide has unique electrocatalytic behavior for CO₂ reduction and the formation of reduction products. It is important to highlight that carbon dioxide reduction does not proceed when a bare FTO conducting glass electrode is used.

To determinate the nature of the currents associated with CO₂ electrocatalytic reduction, a linear sweep voltammetry (LSV) was performed. At a relatively low scan rate (5 mV·s⁻¹), the capacitive current decreases, and the faradaic currents are mainly observed. Figure 2 shows the initial potential at which the cathodic current for CO₂ reduction appears, providing further evidence on the faradaic nature of the cathodic currents linked to CO₂ reduction. However, the presence of CO₂ generates changes in current profiles, and not only produces faradaic currents due to CO₂ reduction, but also increases capacitive currents due to the formation of electron-rich centers in reduced metal species. Therefore, to determinate the potential at which the faradaic process starts for the metal oxide materials studied, a double potential step chronoamperometry experiment was performed. A potential step was performed from the 1.0 V as initial potential (Pi), at which no faradaic process occurs, to several negative final potentials (Pf). Each step was applied for 59 s.

The chronoamperometric profiles shown in Figure 3 indicate the potential steps associated with each thin-film electrode. For MoO₃, when the applied potential returns to Pi, the current in both CO₂ and N₂ purged is the same. In contrast, after electrode polarization to the initial potential from each final potential with CO₂ electrode saturation, Fe₂O₃ shows an increase in anodic current. This could possibly be related to a reduction product reoxidation. In this sense, it is worth nothing that a wide potential peak at 0.2 V is observed, as can be seen from the cyclic voltammetry results. When a negative potential was applied under N₂ and CO₂ purging conditions, the currents were not always the same at the end of each step potential. For Fe₂O₃, an increase in current is observed from -0.3 V after 59 s under CO₂ purge conditions, the increase being higher at -0.5 V. For MoO₃, said increase in current becomes evident at -0.7 V.

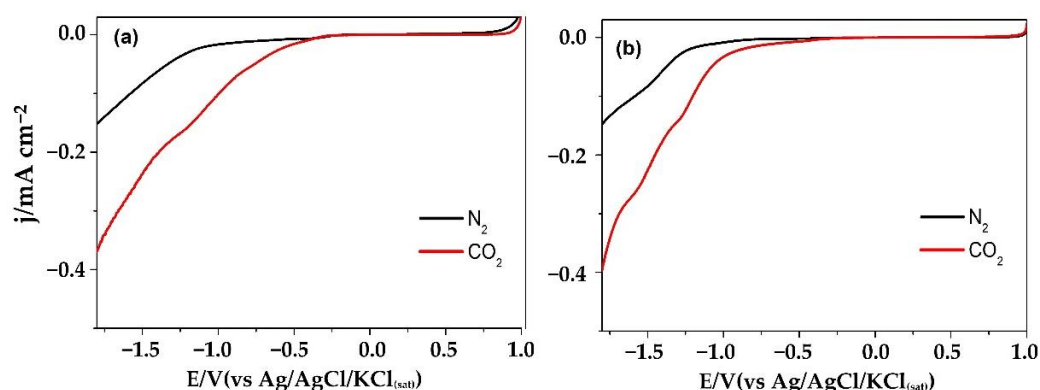


Figure 2. Linear sweep voltammograms taken in 0.1 M TBAF/ACN with TMO thin-film electrodes at $5 \text{ mV}\cdot\text{s}^{-1}$ scanning rate: (a) Fe_2O_3 , (b) MoO_3 . The black and red curves correspond to scans under an atmosphere of N_2 and CO_2 , respectively.

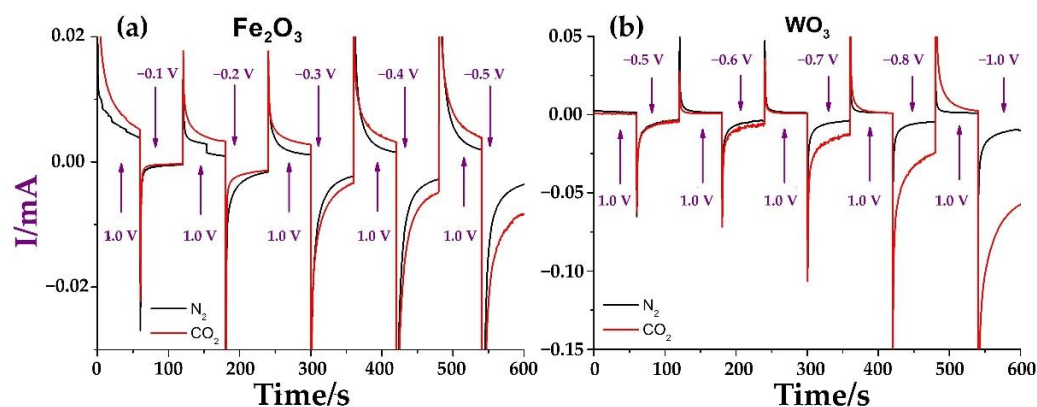


Figure 3. Double potential step chronoamperometry results for the electrocatalytic reduction of CO_2 in 0.1 M TBAF/ACN electrolyte solution with thin-film electrodes: (a) Fe_2O_3 and (b) MoO_3 . The red and black graphs correspond to the electrolyte purged with N_2 and CO_2 , individually. Blue arrow corresponds to initial potential (P_i). Arrows indicate potential steps.

Under CO_2 and N_2 bubbling conditions, the absolute value of the difference between observed currents as a function of the applied potential step is defined by Equation (9):

$$|j_{\text{CO}_2\text{max}} - j_{\text{N}_2\text{max}}| (\text{V}) = |j_{\text{CO}_2\text{max}(v)}| - |j_{\text{N}_2\text{max}(v)}| \quad (9)$$

where $|j_{\text{CO}_2\text{max}(v)}|$ and $|j_{\text{N}_2\text{max}(v)}|$ are the cathodic currents obtained 59 s after the electrode polarization occurs at the potential P_f .

A current profile calculated using Equation (9) has an increase in the relationship between faradaic and non-faradaic currents, as shown in Figure 4. In each case, the intercept with the potential axis corresponds to the onset potential for faradaic current related with the CO_2 reduction. The onset for electrodes used in this study was -0.4 V for Fe_2O_3 , and -0.6 V for MoO_3 . Furthermore, Figure 4 reveals not only the decrease of the overpotential for CO_2 reduction, but also the higher faradaic currents for the Fe_2O_3 electrode, being the best electrocatalytic electrode under the experimental conditions. It should be noted that differences in electrode interface area may vary and are desirable for proper electrode performance comparison.

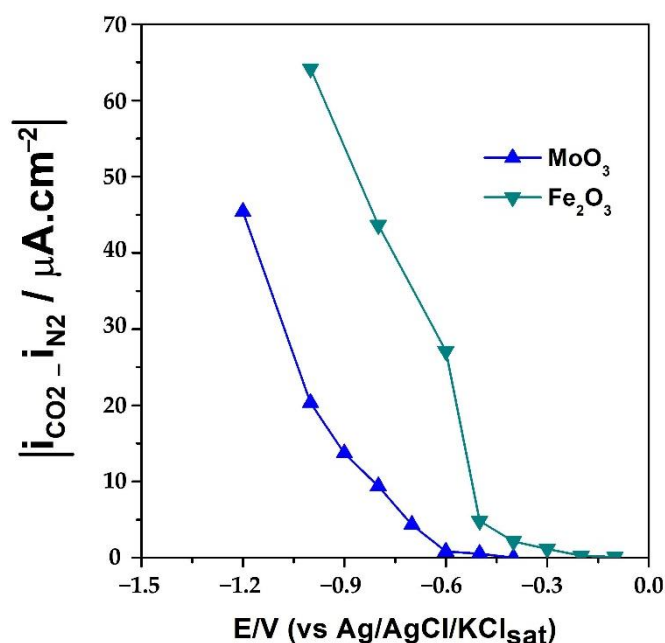
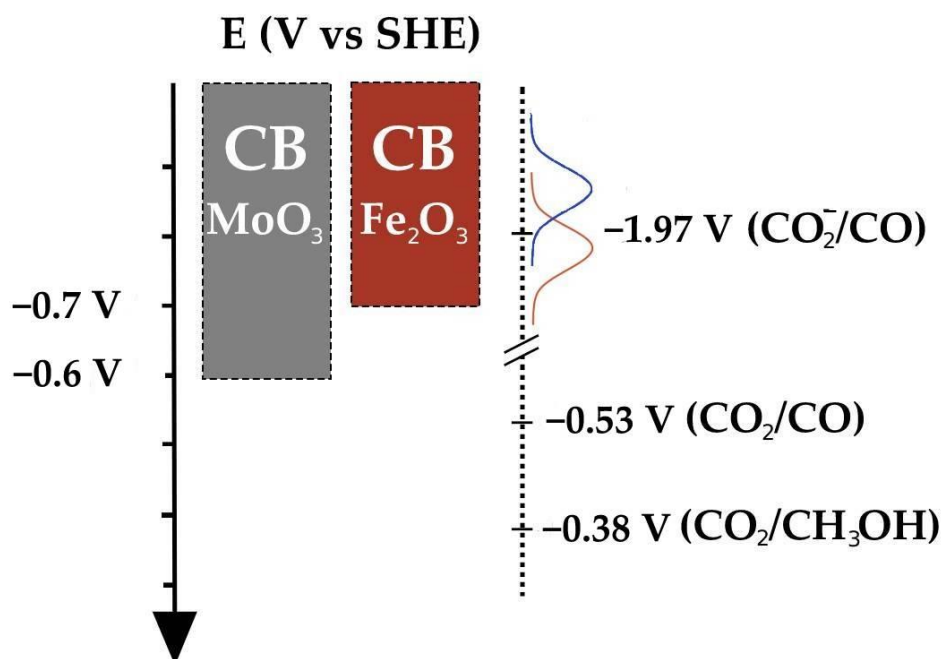


Figure 4. Profile of current associated with CO₂ reduction faradaic processes for examined TMO materials as a function of applied potential in square-wave chronoamperometric experiments.

On the other hand, TMOs, such as Fe₂O₃ and MoO₃, are n-type semiconductors, and their catalytic activity could be related to the conduction band position [32]. The conduction band position could estimate if the electron transfer is thermodynamically feasible. Although several conduction and valence band position diagrams are found in literature for the thin film electrodes studied, these values correspond to conditions different from those applied in this study, and are generally under vacuum conditions [33]. However, the potential at which the conduction band is found depends on factors such as the type of oxide, charge state of the surface, presence of adsorbed species, pH, and isoelectric point of the material [34]. In this way, the flat band potential was estimated via photoelectrochemical measurements in the presence of low oxidation potential species such as methanol [35]. This potential should be very close to the potential of the conduction band lower edge, and related with the apparition of photocurrents. Figure S5 in Supporting Information shows the LSV profile for Fe₂O₃ and MoO₃ electrodes under transitory illumination, in 0.1 M de TBAF/ACN/+3.0 M CH₃OH, purged with N₂. The results show that photocurrent onset potentials start at −0.70 V for Fe₂O₃, and 0.65 V for MoO₃. Therefore, the electron transference from the TMO to CO₂ molecule and the formation of thermodynamically favored C₁ products from CO₂ reduction are feasible. Scheme 1 represents the conduction band position for TMO under the conditions of this study, and the potentials (versus SHE at pH 7) for some relevant CO₂ redox couples (Scheme 1).

The results show a generalized catalytic behavior for CO₂ electrocatalytic reduction over the TMO electrodes used. In all cases, a decrease in the overpotential related to that required for the first CO₂ electron transfer is evident. According to the dissociative reduction model, in the presence of CO₂, the formation of OV caused by the application of increasingly negative potentials appears to be favored by the stabilization of Fe²⁺ and Mo⁵⁺ species upon CO₂ chemisorption. Therefore, it is plausible to think that CO₂ could be adsorbed in reduced metal sites, and that the OV generation is favored. Metal reduction is facilitated, causing an increase in capacitive currents in CV profiles, even at potentials where CO₂ reduction does not proceed. In this sense, it is reasonable to think that the catalytic surface of the examined TMO materials possesses a different morphology and adsorption energy for CO₂, and, therefore, a different activation capability [11,36,37]. Likewise, Tanabe et al. found that basic metal oxides facilitate the transfer of electrons to CO₂ molecules adsorbed on the surface by adduct formation [38].



Scheme 1. Representation of the conduction band position measured by flat band potential determination and some CO₂ redox couples related with the onset of the faradic currents.

Although the activation of the CO₂ molecule by adsorption on the surface of the catalyst favors its reduction, it is not the only factor that determines the electrocatalytic activity of the electrode. The formation of the adsorbed surface does not always lead to CO₂ reduction [36]. In this sense, it is important to consider the need of electron-rich active sites giving rise to electron transfer from the TMO surface to the CO₂ molecule. Thus, the formation of reduced sites identified as catalytic sites for the reduction of CO₂ occurs [21,39]. Density Functional Theory calculations show that OV with n-type semiconductor behavior enhance the surface state near the conduction band [40]. Based on the results obtained, the increment of surface states improves the electrode catalytic activity even at potentials at which CO₂ reduction does not occur.

Finally, conduction band position, OV density and their associated energy, as well as surface state density are parameters needed to understand the electrocatalytic behavior of TMO materials. Table 1 presents the initial flat band and faradaic current potentials, E_{fb} and E_{fi} , for the electrocatalytic reduction of CO₂.

Table 1. Initial and flat band potential for TMO electrodes. Potentials were measured versus an Ag/AgCl/KCl_{sat} reference electrode.

Electrode	E/V (E_{fb})	E/V (E_{fi})
Fe ₂ O ₃	−0.70	−0.4
WO ₃	−0.50	−0.6
MoO ₃	−0.60	−0.6
TiO ₂	−1.55	−1.3

The initial faradaic onset potential for Fe₂O₃ electrodes is less negative than those at the the conduction band position. This fact reveals a high density of surface states near the conduction band; from which, electron transfer to the adsorbed CO₂ molecules occurs. In the case of MoO₃, E_{fb} and E_{fi} are very close to each other. The initial potential for MoO₃ is 0.05 V, which is less negative than its flat band potential. This could be related to the fact that the metal Mo has different oxidation numbers; therefore, the excess charge from the formation of OV can be distributed on both surface and bulk atoms, causing the excess charge to delocalize, and the density of electron-rich sites to decrease. The migration

capability for OV in TMO such as TiO_2 and WO_3 is predicted by DFT studies, as well as (0 0 1)-orientation activation energies of 0.76 V and 0.14 V, respectively [41,42]. This means that excess electrons resulting from OV formation in TMO such as MoO_3 may migrate to the bulk structure more seamlessly than Fe_2O_3 [43], which suggests a greater availability of Lewis basic active sites on the TMO surface for CO_2 reduction when the OV migration energy is higher.

3. Materials and Methods

The preparation of Fe_2O_3 and MoO_3 electrodes was carried out by chemical bath deposition and the sol-gel method, respectively [28]. Experimental details for oxide thin-film synthesis and the characterization are presented in the Supporting Information.

A computer-controlled micro-Autolab potentiostat was used for all electrochemical experiments. A conventional three-electrode glass cell was used with an $\text{Ag}/\text{AgCl}(\text{s})/\text{KCl}(\text{aq}, \text{sat})$ reference electrode and a Pt wire as a counter electrode in all the experiments. The supporting electrolyte was 0.1 M tetrabutylammonium perchlorate (TBAP) ($\geq 99.0\%$ from Sigma-Aldrich, Madrid, Spain) in ACN (99.88% anhydrous from Scharlau, Multisolvent, HPLC grade, Barcelona, Spain). In all the experiments, the electrolyte was purged for 30 min with either N_2 (Alphagaz 99.999%, Madrid, Spain) or CO_2 (Air Liquid, 99.98%, Madrid, Spain). A conversion of potentials measured to SHE scale is the same as previously reported, and according to Pavlishchuk and Addison. Detailed information about materials, methods, and the potential conversion scale are presented in the Supporting Information.

4. Conclusions

Based on the results obtained, TMOs present an electrocatalytic behavior for the reduction of CO_2 in ACN medium. In this sense, it could be affirmed that the location of the conduction band, the ability to generate OV, and charge accumulation in surface states are factors that can modify the charge transfer from TMO to CO_2 . The results obtained show that, in general terms, the less negative (in potential) the conduction band position is, the more positive the potential at which the processes of faradic reduction of CO_2 are initiated. This behavior is expected, since there is a correlation between the location of the edge of the conduction band and the electronic surface states responsible for the CO_2 activation. In this sense, future studies that allow obtaining information on the generation energy and the migration of OVs may be relevant for the evaluation of a TMO as a possible (photo)cathode for CO_2 reduction. Finally, it should be noted that carbon monoxide was obtained as a reduction product, which is in accordance with what is expected for aprotic systems.

Supplementary Materials: The following supporting information can be downloaded at: <https://www.mdpi.com/article/10.3390/ijms232113367/s1>. References [44,45] are cited in the Supplementary Materials.

Author Contributions: Conceptualization, N.E.M.-R. and C.A.G.-F.; methodology, N.E.M.-R. and A.S.L.-P.; formal analysis, N.E.M.-R. and A.S.L.-P.; investigation, N.E.M.-R.; data curation, A.S.L.-P.; writing—original draft preparation, A.S.L.-P.; writing—review and editing, N.E.M.-R.; supervision, C.A.G.-F.; project administration, C.A.G.-F. All authors have read and agreed to the published version of the manuscript.

Funding: This research was funded by MINCIENCIAS through National Doctoral Scholarship (567-2019), and (848-2019) postdoctoral fellowship.

Institutional Review Board Statement: Not applicable.

Informed Consent Statement: Not applicable.

Data Availability Statement: Not applicable.

Acknowledgments: We would like to acknowledge the support of the Universidad Nacional de Colombia, its facilities, and the use of its equipment.

Conflicts of Interest: The authors declare no conflict of interest.

References

1. Sinsel, S.R.; Riemke, R.L.; Hoffmann, V.H. Challenges and solution technologies for the integration of variable renewable energy sources—A review. *Renew. Energy* **2020**, *145*, 2271–2285. [[CrossRef](#)]
2. Kondratenko, E.V.; Mul, G.; Baltrusaitis, J.; Larrazábal, G.O.; Pérez-Ramírez, J. Status and perspectives of CO₂ conversion into fuels and chemicals by catalytic, photocatalytic and electrocatalytic processes. *Energy Environ. Sci.* **2013**, *6*, 3112–3135. [[CrossRef](#)]
3. Lv, J.; Yin, R.; Zhou, L.; Li, J.; Kikas, R.; Xu, T.; Wang, Z.; Jin, H.; Wang, X.; Wang, S. Microenvironment Engineering for the Electrocatalytic CO₂ Reduction Reaction. *Angew. Chem. Int. Ed.* **2022**, *61*, e202207252. [[CrossRef](#)] [[PubMed](#)]
4. Moura de Salles Pupo, M.; Kortlever, R. Electrolyte Effects on the Electrochemical Reduction of CO₂. *ChemPhysChem* **2019**, *20*, 2926–2935. [[CrossRef](#)]
5. Ait Ahsaine, H.; Zbair, M.; BaQais, A.; Arab, M. CO₂ Electroreduction over Metallic Oxide, Carbon-Based, and Molecular Catalysts: A Mini-Review of the Current Advances. *Catalysts* **2022**, *12*, 450. [[CrossRef](#)]
6. Yang, J.H.; Park, S.J.; Rhee, C.K.; Sohn, Y. Photocatalytic CO₂ Reduction and Electrocatalytic H₂ Evolution over Pt(0,II,IV)-Loaded Oxidized Ti Sheets. *Nanomaterials* **2020**, *10*, 1909. [[CrossRef](#)]
7. Zhang, Q.; Li, Y.; Zhu, H.; Suo, B. High-Performance of Electrocatalytic CO₂ Reduction on Defective Graphene-Supported Cu₄S₂ Cluster. *Catalysts* **2022**, *12*, 454. [[CrossRef](#)]
8. Tackett, B.M.; Gomez, E.; Chen, J.G. Net reduction of CO₂ via its thermocatalytic and electrocatalytic transformation reactions in standard and hybrid processes. *Nat. Catal.* **2019**, *2*, 381–386. [[CrossRef](#)]
9. Xu, S.; Carter, E.A. Theoretical Insights into Heterogeneous (Photo)electrochemical CO₂ Reduction. *Chem. Rev.* **2018**, *119*, 6631–6669. [[CrossRef](#)]
10. Freund, H.J.; Roberts, M. Surface chemistry of carbon dioxide. *Surf. Sci. Rep.* **1996**, *25*, 225–273. [[CrossRef](#)]
11. Indrakanti, V.P.; Kubicki, J.D.; Schobert, H.H. Photoinduced activation of CO₂ on Ti-based heterogeneous catalysts: Current state, chemical physics-based insights and outlook. *Energy Environ. Sci.* **2009**, *2*, 745–758. [[CrossRef](#)]
12. Lamy, E.; Nadjó, L.; Savéant, J.M. Standard potential and kinetic parameters of the electrochemical reduction of carbon dioxide in dimethylformamide. *J. Electroanal. Chem. Interfacial Electrochem.* **1977**, *78*, 403–407. [[CrossRef](#)]
13. Koppenol, W. Oxyradical reactions: From bond-dissociation energies to reduction potentials. *FEBS Lett.* **1990**, *264*, 165–167. [[CrossRef](#)]
14. Shah, S.S.A.; Sufyan Javed, M.; Najam, T.; Molochas, C.; Khan, N.A.; Nazir, M.A.; Xu, M.; Tsiakaras, P.; Bao, S.J. Metal oxides for the electrocatalytic reduction of carbon dioxide: Mechanism of active sites, composites, interface and defect engineering strategies. *Coord. Chem. Rev.* **2022**, *471*, 214716. [[CrossRef](#)]
15. Rasko, J.; Solymosi, F. Infrared Spectroscopic Study of the Photoinduced Activation of CO₂ on TiO₂ and Rh/TiO₂ Catalysts. *J. Phys. Chem.* **1994**, *98*, 7147–7152. [[CrossRef](#)]
16. Perissinotti, L.L.; Brusa, M.A.; Grela, M.A. Yield of Carboxyl Anion Radicals in the Photocatalytic Degradation of Formate over TiO₂ Particles. *Langmuir* **2001**, *17*, 8422–8427. [[CrossRef](#)]
17. Habisreutinger, S.N.; Schmidt-Mende, L.; Stolarczyk, J.K. Photocatalytic Reduction of CO₂ on TiO₂ and Other Semiconductors. *Angew. Chem. Int. Ed.* **2013**, *52*, 7372–7408. [[CrossRef](#)] [[PubMed](#)]
18. Ludwig, T.; Singh, A.R.; Nørskov, J.K. Acetonitrile Transition Metal Interfaces from First Principles. *J. Phys. Chem. Lett.* **2020**, *11*, 9802–9811. [[CrossRef](#)]
19. Gomes, R.J.; Birch, C.; Cencer, M.M.; Li, C.; Son, S.B.; Bloom, I.D.; Assary, R.S.; Amanchukwu, C.V. Probing Electrolyte Influence on CO₂ Reduction in Aprotic Solvents. *J. Phys. Chem. C* **2022**, *126*, 13595–13606. [[CrossRef](#)]
20. Kunttyi, R.; Zozulya, G.; Shepida, M. CO₂ Electroreduction in Organic Aprotic Solvents: A Mini Review. *J. Chem.* **2022**, *2022*, 1306688. [[CrossRef](#)]
21. Bandi, A. Electrochemical Reduction of Carbon Dioxide on Conductive Metallic Oxides. *J. Electrochem. Soc.* **1990**, *137*, 2157–2160. [[CrossRef](#)]
22. Chu, S.; Yan, X.; Choi, C.; Hong, S.; Robertson, A.W.; Masa, J.; Han, B.; Jung, Y.; Sun, Z. Stabilization of Cu⁺ by tuning a CuO–CeO₂ interface for selective electrochemical CO₂ reduction to ethylene. *Green Chem.* **2020**, *22*, 6540–6546. [[CrossRef](#)]
23. Lum, Y.; Ager, J.W. Stability of Residual Oxides in Oxide-Derived Copper Catalysts for Electrochemical CO₂ Reduction Investigated with ¹⁸O Labeling. *Angew. Chem. Int. Ed.* **2017**, *57*, 551–554. [[CrossRef](#)]
24. Zou, Y.; Wang, S. An Investigation of Active Sites for electrochemical CO₂ Reduction Reactions: From In Situ Characterization to Rational Design. *Adv. Sci.* **2021**, *8*, 2003579. [[CrossRef](#)]
25. Figueiredo, M.C.; Ledezma-Yanez, I.; Koper, M.T.M. In Situ Spectroscopic Study of CO₂ Electroreduction at Copper Electrodes in Acetonitrile. *ACS Catal.* **2016**, *6*, 2382–2392. [[CrossRef](#)]
26. Rudnev, A.V.; Zhumaev, U.E.; Kuzume, A.; Vesztergom, S.; Furrer, J.; Broekmann, P.; Wandlowski, T. (The promoting effect of water on the electroreduction of CO₂ in acetonitrile. *Electrochim. Acta* **2016**, *189*, 38–44. [[CrossRef](#)]
27. de Castro, I.A.; Datta, R.S.; Ou, J.Z.; Castellanos-Gomez, A.; Sriram, S.; Daeneke, T.; Kalantar-Zadeh, K. Molybdenum Oxides—From Fundamentals to Functionality. *Adv. Mater.* **2017**, *29*, 1701619. [[CrossRef](#)]
28. Mendieta-Reyes, N.E.; Díaz-García, A.K.; Gómez, R. Simultaneous Electrocatalytic CO₂ Reduction and Enhanced Electrochromic Effect at WO₃ Nanostructured Electrodes in Acetonitrile. *ACS Catal.* **2018**, *8*, 1903–1912. [[CrossRef](#)]
29. Masetti, E.; Dini, D.; Decker, F. The electrochromic response of tungsten bronzes MxWO₃ with different ions and insertion rates. *Sol. Energy Mater. Sol. Cells* **1995**, *39*, 301–307. [[CrossRef](#)]

30. Foley, J.K.; Korzeniewski, C.; Pons, S. Anodic and cathodic reactions in acetonitrile/tetra-n-butylammonium tetrafluoroborate: An electrochemical and infrared spectroelectrochemical study. *Can. J. Chem.* **1988**, *66*, 201–206. [[CrossRef](#)]
31. Hepel, M.; Wickham, D. Large Cation Model of Dissociative Reduction of WO_{3-x} Lattice Studied by EQCN and AFM. *ECS Trans.* **2009**, *19*, 11–23. [[CrossRef](#)]
32. Chava, R.K.; Son, N.; Kang, M. Band structure alignment transitioning strategy for the fabrication of efficient photocatalysts for solar fuel generation and environmental remediation applications. *J. Colloid Interface Sci.* **2022**, *627*, 247–260. [[CrossRef](#)]
33. Jian, J.; Sun, J. A Review of Recent Progress on Silicon Carbide for Photoelectrochemical Water Splitting. *Sol. RRL* **2020**, *4*, 2000111. [[CrossRef](#)]
34. Wang, D.; Liu, Z.P.; Yang, W.M. Proton-Promoted Electron Transfer in Photocatalysis: Key Step for Photocatalytic Hydrogen Evolution on Metal/Titania Composites. *ACS Catal.* **2017**, *7*, 2744–2752. [[CrossRef](#)]
35. Ismael, M. Highly effective ruthenium-doped TiO_2 nanoparticles photocatalyst for visible-light-driven photocatalytic hydrogen production. *New J. Chem.* **2019**, *43*, 9596–9605. [[CrossRef](#)]
36. Breyer, C.; Reichert, D.; Seidel, J.; Hüttel, R.; Mertens, F.; Kureti, S. Kinetic modeling of the adsorption and desorption of CO_2 on $\alpha\text{-Fe}_2\text{O}_3$. *Phys. Chem. Chem. Phys.* **2015**, *17*, 27011–27018. [[CrossRef](#)]
37. Liu, L.; Lin, M.; Liu, Z.; Sun, H.; Zhao, X. Density functional theory study of CO_2 and H_2O adsorption on a monoclinic $\text{WO}_3(001)$ surface. *Chem. Res. Chin. Univ.* **2017**, *33*, 255–260. [[CrossRef](#)]
38. Wicke, E.J.R., Anderson, M., Boudart. (Eds.): Catalysis, Science and Technology. Vol. 4, Springer-Verlag, Berlin, Heidelberg, New York 1983. 289 Seiten, Preis: DM 132,-. *Ber. Bunsenges. Phys. Chem.* **1984**, *88*, 586. [[CrossRef](#)]
39. Rao, C.N.R. Transition Metal Oxides. *Annu. Rev. Phys. Chem.* **1989**, *40*, 291–326. [[CrossRef](#)]
40. Di Valentin, C.; Pacchioni, G.; Selloni, A. Reduced and n-Type Doped TiO_2 : Nature of Ti^{3+} Species. *J. Phys. Chem. C* **2009**, *113*, 20543–20552. [[CrossRef](#)]
41. Cheng, H.; Selloni, A. Energetics and diffusion of intrinsic surface and subsurface defects on anatase $\text{TiO}_2(101)$. *J. Chem. Phys.* **2009**, *131*, 054703. [[CrossRef](#)] [[PubMed](#)]
42. Le, H.M.; Vu, N.H.; Phan, B.T. Migrations of oxygen vacancy in tungsten oxide (WO_3): A density functional theory study. *Comput. Mater. Sci.* **2014**, *90*, 171–176. [[CrossRef](#)]
43. Yin, W.J.; Wen, B.; Zhou, C.; Selloni, A.; Liu, L.M. Excess electrons in reduced rutile and anatase TiO_2 . *Surf. Sci. Rep.* **2018**, *73*, 58–82. [[CrossRef](#)]
44. Hasani-Sadrabadi, M.M.; Dashtimoghadam, E.; Nasserri, R.; Karkhaneh, A.; Majedi, F.S.; Mokarram, N.; Renaud, P.; Jacob, K.I. Cellulose nanowhiskers to regulate the microstructure of perfluorosulfonate ionomers for high-performance fuel cells. *J. Mater. Chem. A* **2014**, *2*, 11334. [[CrossRef](#)]
45. Pavlishchuk, V.V.; Addison, A.W. Conversion constants for redox potentials measured versus different reference electrodes in acetonitrile solutions at 25 °C. *Inorg. Chim. Acta* **2000**, *298*, 97–102. [[CrossRef](#)]